Research Article | Vol. 30, No. 9 / 25 Apr 2022 / Optics Express 15546
Optics EXPRESS

Non-classical high harmonic generation in graphene driven by linearly-polarized laser pulses

ROBERTO BOYERO-GARCÍA,* ANA GARCÍA-CABRERA, OSCAR ZURRÓN-CIFUENTES, CARLOS HERNÁNDEZ-GARCÍA, AND LUIS PLAJA

Grupo de Investigación en Aplicaciones del Láser y Fotónica, Departamento de Física Aplicada, Universidad de Salamanca, E- 37008, Salamanca, Spain
robertobg@usal.es

Abstract: Recent studies in high-order harmonic generation (HHG) in solid targets reveal new scenarios of extraordinary rich electronic dynamics, in comparison to the atomic and molecular cases. For the later, the main aspects of the process can be described semiclassically in terms of electrons that recombine when the trajectories revisit the parent ion. HHG in solids has been described by an analogous mechanism, in this case involving electron-hole pair recombinations. However, it has been recently reported that a substantial part of the HHG emission corresponds to situations where the electron and hole trajectories do not overlap in space. According to the present knowledge, HHG from this *imperfect* recollisions reflects the quantum nature of the process, arising in systems with large Berry curvatures or for elliptically polarized driving fields. In this work, we demonstrate that *imperfect* recollisions are also relevant in the more general case. We show the signature of such recollisions in the HHG spectrum from monolayer graphene —a system with null Berry curvature— irradiated by linearly polarized driving fields. Our calculations also reveal that *imperfect* multiple-order recollisions contribute to the harmonic emission when electron-hole excursion times exceed one cycle of the driving field. We believe that our work adds a substantial contribution to the full understanding of the sub-femtosecond dynamics of HHG in solid systems.

1. Introduction

High-harmonic generation (HHG) is nowadays a well established technique to generate highly coherent extreme-ultraviolet/x-ray radiation [1–7]. The phenomenon stems from the non-perturbative interaction of intense laser light with matter. For atomic and molecular targets, HHG can be understood in semiclassical terms, according to the so-called three-step model [8]. In this point of view, harmonics are radiated when a tunnel-ionized electron returns to the parent ion, where it recombines releasing its kinetic energy in the form of high-frequency radiation. This later step is only efficient if the electron's trajectory returns to the parent ion, which is a condition naturally found in linearly-polarized driving fields. For elliptically-polarized drivers, the electrons are pulled away from the parent ion, and the efficiency of the HHG process decreases accordingly [9]. It is worth noticing also that the electron may not recombine at the first encounter with the parent ion, therefore the harmonics can be emitted at subsequent *higher-order* recollisions [10–12]. In such case, however, the radiated photon energies fall well below the maximum photon energy of the first recollisions (the so-called harmonic *cutoff* frequency). Moreover, since high-order recollisions imply electron's excursion times longer than the driver's cycle, they are associated to lower harmonic conversion efficiencies, resulting from the progressive spread of the electron's wavepacket in the continuum [13–15].

#452201 https://doi.org/10.1364/OE.452201
Journal © 2022 Received 23 Dec 2021; revised 22 Feb 2022; accepted 7 Apr 2022; published 21 Apr 2022

Optics EXPRESS

Solid targets provide richer scenarios for HHG [6,16–21]. In this case, the irradiation geometry defines the HHG mechanism. For grazing incidences, i.e. when the polarization plane of the driving electric field is perpendicular to the target's surface, HHG follows from the recombination of electrons detached from the target [22], in close resemblance to the ionization mechanism in atomic and molecular cases. For solid targets, however, the crystal periodicity leaves a signal in the detached electron's wavefunction, in form of Talbot modulations, which in turn are reflected in the HHG spectrum. This phenomenon gives ground to the recent proposal of ultrafast Talbot spectroscopy at the nanometer scale [23]. On the other hand, for the case of normal incidence or bulk solid targets, the HHG mechanism follows from an adapted semiclassical three-step model [24]. According to this view, the electron's tunnel ionization step is replaced by tunnel excitation to the conduction band, and the consequent creation of a hole. Harmonics result from the electron-hole recombination at times when the electron and hole trajectories overlap, i.e. the so called *perfect recollisions* (ehPR). As a main characteristic, the harmonic *cutoff* frequency corresponds to the maximum energy gap during the electron/hole excursion [24–28].

Despite of these fundamental similarities, HHG in solids turns out to be far more complex than in atoms and molecules. On the one side, the crystal band's dispersion is not quadratic and thus, the dynamics of the electron in the conduction band is not as trivial as that of an electron ionized in free space. In addition, Berry curvatures introduce a deflection in the electron and hole trajectories. Therefore, while in gas systems the electron trajectories are universally defined, in solids they depend on the target species. On the other side, the details of the excitation of the electron to the conduction band are also affected by the band structure. For instance, it has been demonstrated that HHG from elliptically-polarized drivers results from electrons tunnel-excited at points surrounding the minimum band gap, rather than at the exact point [29]. In 2D semimetals enclosing Dirac points, the excitation details are more involved, as tunneling is replaced by the non-adiabatic crossing near these singular points [30]. This simple variation in the first step leads to substantial differences in the HHG process, as electron-hole excitation is no longer linked to the maxima of the driving field's amplitude. In other low dimensional targets, as carbon nanotubes, HHG follows from a similar non-adiabatic excitation mechanism near the Van Hove singularities [31].

In the general case, the complex dynamics in crystals does not only affect the maximum photon's energy but also the polarization and phase properties of the emitted harmonics. In particular, the band geometry around the symmetry points can lead to a highly non-linear anisotropic response, resulting in the generation of harmonics with elliptical polarization even when driven by linearly-polarized drivers [22,32–41]. In addition, the convoluted electronic dynamics during HHG in solids leads to high harmonics with complex phase properties. As a result, accounting for the spatial phase distribution in HHG from a macroscopic target [26,42] has allowed to achieve a better understanding of the harmonic spectrum properties.

It has been recently shown that although the modified semiclassical three-step model accounts for the main features of the HHG mechanism in solids, non-classical pathways can be also relevant in systems with large Berry curvatures [43] or when HHG is driven by elliptically polarized fields [44]. In these cases, harmonics are emitted during electron-hole *imperfect recollisions* (ehIR), i.e. when the electron-hole wave packets overlap even though their centers are spatially separated by distances one order of magnitude larger than the lattice constant [43].

In this article, we demonstrate that ehIR's have a relevant role also for HHG in solids with vanishing Berry curvature and driven by linearly-polarized laser fields. In particular, we show the enhanced role of high-order ehIR at times larger than the laser cycle. The excellent agreement between our semiclassical and quantum calculations demonstrates that ehIR must be considered to obtain a better understanding of the complex phase properties of HHG in solids.

The article is organized as follows. In Section 2, we present the details of the computation of the nonlinear response, where we use two models: the resolution of the time dependent

Optics EXPRESS

Schrödinger equation within the first neighbor tight-binding approximation, and a semiclassical saddle-point approach which allow us to interpret our results. In Section 3, we present and discuss our findings, where we identify the role of ehPR and ehIR for several cases of HHG in single-layer graphene driven by a linearly-polarized laser field. Finally we present our conclusions in Section 4.

2. Theoretical description of HHG in single-layer graphene

We consider the emission of high-order harmonics in single-layer graphene irradiated by a short mid-infrared pulse, linearly polarized along the graphene sheet plane. To this end, we compute the nonlinear response of graphene following the method described in [30], and we interpret our results in terms of classical electron-hole trajectories in real space. The dynamics of the interaction of a single layer graphene sheet with an ultrashort laser pulse will be described in the first neighbor tight-binding approximation [45]. We express the electron wavefuntion in terms of the graphene's eigenstates, $\Phi^{\pm}_{\mathbf{k}}(\mathbf{r})$,

$$\Psi(\mathbf{r},t) = \int \Psi_{\mathbf{k}}(\mathbf{r},t)d\mathbf{k} = \int \left[C_+(\mathbf{k},t)\Phi^+_{\mathbf{k}}(\mathbf{r}) + C_-(\mathbf{k},t)\Phi^-_{\mathbf{k}}(\mathbf{r})\right] d\mathbf{k}. \tag{1}$$

with $\Phi^{\pm}_{\mathbf{k}}(\mathbf{r})$ given as vectors in the basis of Bloch states,

$$\Phi^{\pm}_{\mathbf{k}}(\mathbf{r}) = \sqrt{\frac{1}{2}} e^{i\mathbf{k}\cdot\mathbf{r}} \begin{pmatrix} \pm 1 \\ e^{-i\phi(\mathbf{k})} \end{pmatrix}, \tag{2}$$

$\phi(\mathbf{k})$ being the argument of the complex function $f(\mathbf{k})$,

$$f(\mathbf{k}) = e^{-iak_x/\sqrt{3}} \left(1 + 2e^{i\sqrt{3}ak_x/2} \cos\frac{ak_y}{2}\right), \tag{3}$$

where $a = 2.46$Å.

The evolution of $\Psi(\mathbf{r},t)$ is solved in the reciprocal space's moving frame $\hbar\boldsymbol{\kappa}_t = \hbar\mathbf{k} - q_e\mathbf{A}(t)/c$, where $\mathbf{A}(t)$ is the vector potential of the electromagnetic field, c the speed of light, and q_e the electron's charge. The numerical instabilities associated with the singularities at the Dirac points can be circumvented by using the change of variables,

$$C_M(\boldsymbol{\kappa}_t,t) = C_+(\boldsymbol{\kappa}_t,t) - C_-(\boldsymbol{\kappa}_t,t) \tag{4}$$

$$C_P(\boldsymbol{\kappa}_t,t) = e^{-i\phi(\boldsymbol{\kappa}_t)}\left[C_+(\boldsymbol{\kappa}_t,t) + C_-(\boldsymbol{\kappa}_t,t)\right], \tag{5}$$

whose temporal dependence is governed by the following equations,

$$i\hbar\frac{d}{dt}C_M(\boldsymbol{\kappa}_t,t) = \frac{E_+(\boldsymbol{\kappa}_t)+E_-(\boldsymbol{\kappa}_t)}{2}C_M(\boldsymbol{\kappa}_t,t) + \frac{E_+(\boldsymbol{\kappa}_t)-E_-(\boldsymbol{\kappa}_t)}{2}e^{i\phi(\boldsymbol{\kappa}_t)}C_P(\boldsymbol{\kappa}_t,t) \tag{6}$$

$$i\hbar\frac{d}{dt}C_P(\boldsymbol{\kappa}_t,t) = \frac{E_+(\boldsymbol{\kappa}_t)+E_-(\boldsymbol{\kappa}_t)}{2}C_P(\boldsymbol{\kappa}_t,t) + \frac{E_+(\boldsymbol{\kappa}_t)-E_-(\boldsymbol{\kappa}_t)}{2}e^{-i\phi(\boldsymbol{\kappa}_t)}C_M(\boldsymbol{\kappa}_t,t) \tag{7}$$

where $E_{\pm}(\mathbf{k}) = \pm\gamma_0|f(\mathbf{k})|$ are the energies of the valence $(-)$ and conduction $(+)$ bands, respectively, and with $\gamma_0 = 2.97$ eV [45].

Finally, by solving Eqs. (6) and (7), we calculate the harmonic emission from the dipole acceleration, $\mathbf{a}(t) = \frac{d^2}{dt^2}\mathbf{d}(t)$ as [30],

$$\mathbf{d}(t) = \langle\Psi(t)|q_e\mathbf{r}|\Psi(t)\rangle = i\frac{q_e}{2}\int \left[C^*_M(\boldsymbol{\kappa}_t,t)\nabla_{\mathbf{k}}C_M(\boldsymbol{\kappa}_t,t) + C^*_P(\boldsymbol{\kappa}_t,t)\nabla_{\mathbf{k}}C_P(\boldsymbol{\kappa}_t,t)\right] d\mathbf{k}. \tag{8}$$

The fundamental physical aspects of HHG in graphene can be revealed by deriving a semiclassical saddle-point approximated model (SPAM), as dicussed in [30]. SPAM considers that the emission

Optics EXPRESS

of the q-th harmonic takes place at time t when the following conditions are fulfilled:

$$E_+(\boldsymbol{\kappa}_t) - E_-(\boldsymbol{\kappa}_t) = q\hbar\omega_0 \tag{9}$$

$$\int_{t_{D,\mathbf{k}}}^{t} \mathbf{v}_+(\boldsymbol{\kappa}_\tau)d\tau = \int_{t_{D,\mathbf{k}}}^{t} \mathbf{v}_-(\boldsymbol{\kappa}_\tau)d\tau \tag{10}$$

where $\mathbf{v}_\pm(\boldsymbol{\kappa}_\tau) = \nabla_{\mathbf{k}} E_\pm(\boldsymbol{\kappa}_\tau)/\hbar$, ω_0 is the laser's fundamental frequency and $t_{D,\mathbf{k}}$ the time when the electron with wave vector $\mathbf{k}$ at the beginning of the interaction crosses the Dirac point, i.e. the time when the electron-hole pair is created. In agreement with the semiclassical description of HHG in solids, SPAM considers that the HHG emission is produced by the recombination of overlapping classical electron-hole trajectories. Note, however, that SPAM describes the evolution of the mean position of the electron and hole wavepackets created in the vicinity of the Dirac points. The excitation of the wavepacket is not resonant with a one photon absorption, but rather is of the Landau-Zenner type during the non-adiabatic crossing near the Dirac points. As a consequence, the pair creation is not confined to the field-amplitude maxima, where tunnel excitation is most likely, but takes place at any time during the interaction. Following the ideas developed in [29,43], in this article we shall demonstrate a substantial role of ehIR in single-layer graphene. Note that this role is unexpected, as graphene is a system with null Berry curvature and our calculations assume that HHG is driven by linearly-polarized laser fields. To include ehIR, we have expanded the SPAM model to take into account the contribution of electron-hole trajectories that do not overlap classically. Therefore, we relax the condition of trajectory crossing in Eq. (10) by allowing the recombination distance ΔR to be nonzero [43],

$$\Delta R \equiv \int_{t_{D,\mathbf{k}}}^{t} \left[\mathbf{v}_+(\kappa_\tau) - \mathbf{v}_-(\kappa_\tau)\right] d\tau \tag{11}$$

Note that this semiclassical approach (SPAM), which does not include the wavepacket dispersion, is just used to interpret the results of the full quantum calculations given by Eqs. (6) and (7).

3. Results and discussion

We consider a six optical cycles (o.c.) driving field with a $\sin^2$ envelope, which corresponds to 2.2 o.c., 22 fs, of full width at half maximum (FWHM) in intensity (see inset in Fig. 1(a)). The field is assumed linearly polarized along the Γ-K direction. The laser pulse is centered at 3 μm wavelength, with a peak intensity of 5×10^{11} W/cm^2, and it is aimed perpendicularly to the graphene's layer. Note that the pulse duration is shorter that the typical electron thermalization time [46]. The resulting harmonic spectrum and its time-frequency analysis are presented in Figs. 1(a) and 1(b), respectively. The time-frequency representation has been obtained scanning over the HHG spectral amplitudes with a Gaussian mask of $4\omega_0$ in FWHM, and subsequently performing the Fourier transform of each sample. As a reference, Figs. 1(c) and 1(d) show the same information for the case of HHG in a hydrogen atom. HHG in hydrogen is calculated from the solution of the three-dimensional time dependent Schrödinger equation, using a 0.72 μm driving field of peak intensity of 1.6×10^{14} W/cm^2, parameters that have been adjusted to produce a HHG spectrum with similar *cutoff* frequency as the graphene case.

The comparison of both spectra reveals that the emission of harmonics in graphene presents a temporal structure far more complex than that in atoms. In the atomic case (Fig. 1(d)) the high-order harmonics result from two well-resolved emission bursts per half-cycle, the so-called short and long trajectories, which present a positive and negative slope structure in the time-frequency representation, respectively [47–51]. In contrast, in HHG from graphene, the first step —the creation of the electron-hole pair— is connected with the Dirac points: electron-hole pair excitation follows from the non-adiabatic crossing near the singular points (see the inset of

Optics EXPRESS

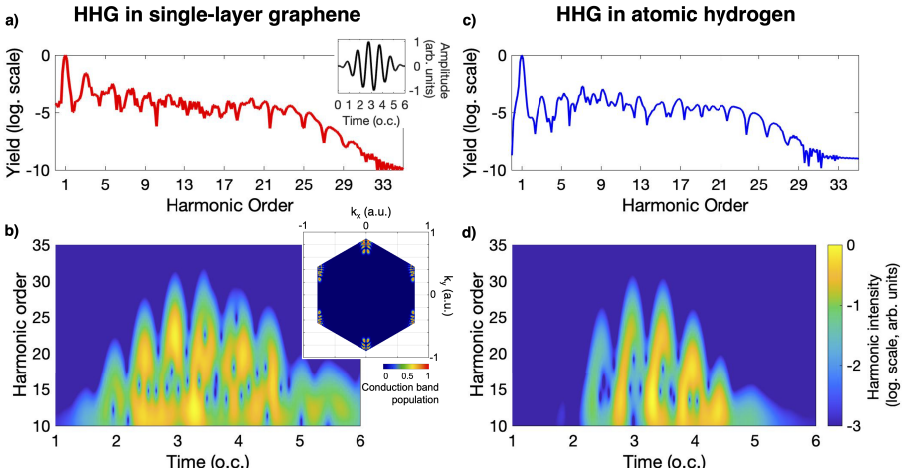

Fig. 1. Harmonic spectrum (a) and time-frequency analysis (b) of the high order harmonic emission from single-layer graphene. The inset in (a) plots the driving electric field, a 3 μm, six-cycles $\sin^2$ pulse (22 fs FWHM) linearly polarized in the graphene plane along the Γ-K direction, with peak intensity of 5×10^{11} W/cm^2. Panels (c) and (d) plot the same information from a hydrogen atom target, irradiated with a linearly-polarized 0.72 μm, six-cycles $\sin^2$ pulse, with peak intensity of 1.6×10^{14} W/cm^2. Inset in (b) is the normalized color map of the electron excitation in the conduction band. The time at which this snapshot is taken is depicted in the inset of panel (a), at 2.75 cycles after the beginning of the laser pulse.

Fig. 1(b)) and, therefore, pairs are created continuously instead of at the driving field's maxima, as it is the general case for bulk crystals, atoms and molecules. As a result, the number of interfering trajectories playing a relevant role in HHG in graphene is substantially larger, and not necessarily regularly spaced in time [30], as it can be observed in Fig. 1(b). Note that, once the driving field interaction with the graphene layer ends, the time-frequency picture reveals that there is still emission from the excited sample, a behavior that has been reported in previous works [36]. In the following we shall see that, even though the semiclassical trajectories leading to ehPR successfully account for the main spectral features in Figs. 1(a) and 1 (b), the harmonic signal can only be fully explained considering also the role of ehIR.

We present in Fig. 2 the results of the SPAM calculations for the graphene case presented in Fig. 1. The background in Figs. 2(a) and 2(b) are replicas of Fig. 1(b). We analyse the temporal distribution of electron-hole recombination energies from ehPR (Fig. 2(a)) and ehIR (Fig. 2(b)). The plotted ehIR energies correspond to the cases in which the electron and hole are 10 unit cells (24 Å, pink lines) and 70 unit cells (172 Å, grey lines) apart, at the instant of recombination. Lighter tones are used for trajectories initiated near the K Dirac points, and darker tones for those initiated near the K′ points (see the inset in Fig. 2(c)). Note that, while the temporal distribution of radiated frequencies from ehPR explains reasonably the fundamental features of the HHG spectrum in (Fig. 2(a)), it becomes also clear that ehPR do not provide a full explanation of the harmonic contributions at intermediate times and, specially, at the end of the driving pulse.

To simplify the discussion of the results from ehIR in Fig. 2(b), we shall focus our attention to the highest harmonic orders, q>15, and to the trajectories originated at the Dirac point K (lighter lines). The discussion of the emission for pairs originated near points K′ (darker lines) is analogous, due to the crystal's inversion symmetry.

Figure 2(b) points out that the emissions from ehIR's for increasingly longer recombination distances are progressively delayed. This is consistent with the increasingly larger excursion times needed for the electron-hole pair to reach longer interparticle distances. This aspect is

Optics EXPRESS

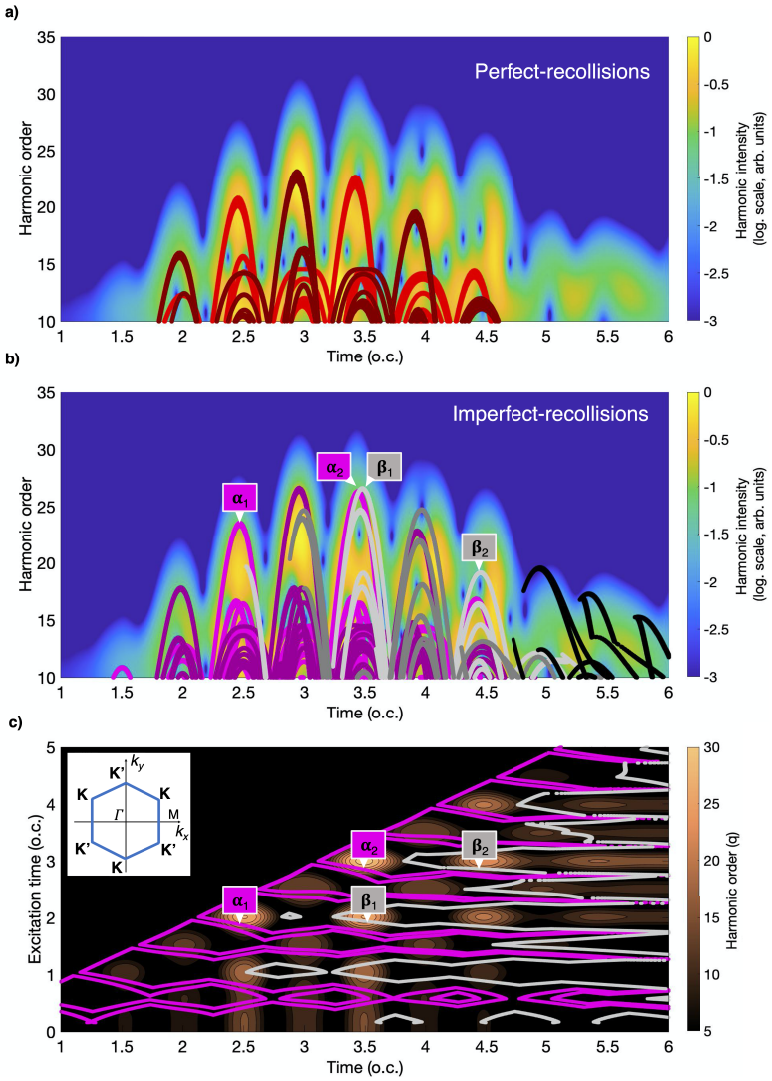

Fig. 2. Results of the harmonic emission corresponding to trajectories leading to ehPR —red, panel (a)— and ehIR —pink and grey, panel (b)—. The electron-hole pairs are created at points K (light colors) and K′ (dark colors) of the graphene's Brillouin zone. Panels (a) and (b) show the energy of the electron-hole pair at recombination obtained with the semiclassical SPAM calculations against the background corresponding to the time-frequency analysis shown in Fig. 1 (b). In (a) we plot the frequency of the harmonic emission corresponding to ehPR, i.e. when the electron and hole classical trajectories intersect, and in (b) the same results for ehIR, where the electron-hole distances at the recombination time are 24 Å (pink) and 172 Å (grey). We have added a long recombination distance of 492 Å (black) in order to recover the harmonic emission at the rear part of the pulse. Panel (c) shows the distribution of energies radiated from ehIR as a function of the pair recombination (horizontal axis) and excitation (vertical axis) times. The inset shows the geometry of graphene's Brillouin zone. Labels α_i and β_i correspond to two pairs of sampled ehIR trajectories recombining at 24 Å and 172 Å, respectively, with excitation times of ∼1.9 o.c. (i=1), and ∼2.9 o.c. (i=2).

Optics EXPRESS

reproduced in Fig. 2(c), where we show the energy of the electron-hole pair at any potential recombination time, as a function of the pair recombination (horizontal axis) and excitation (vertical axis) times. Labels α_i and β_i correspond to two pairs of sampled ehIR trajectories recombining at distances of 24 Å and 172 Å, respectively, with different excitation times: ∼1.9 o.c. for i=1, and ∼2.9 o.c. for i=2. To complete our analysis, we have also included in Fig. 2(b) the trajectory contributions of ehIR that recombine at longer distances (200 unit cells, 492 Å, black lines), which present a relevant contribution at the rear part of the harmonic emission. Thus, our analysis unequivocally demonstrates the relevance of ehIR in HHG in graphene. The harmonic contributions that are not reproduced by ehPR in Fig. 2(a) are mostly fulfilled by the ehIR sampled in Fig. 2(b), whereas the nature of ehIR is clearly identified in Fig. 2(c). We note that a larger sample of ehIR born at different excitation times, and with other recombination distances, completely fulfills the harmonic emmission not reproduced by ehPR in Fig. 2(a).

It is important to point out that the excursion time, i.e. the time lapse between excitation and emission times, increases with the recombination distance. In Ref. [29] ehIR are understood from non-classical pathways, since while the mean position of the electron and hole wavefunctions are distant, dispersion leads to the overlap of the wavefunctions. Threfore, ehIR at larger distances require a larger wavepacket dispersion and, thus, a larger excursion time. Results in Fig. 2(c) show excursion times of the order of 1.5 cycles for ehIR recombining at 172 Å (β_i).

Note that the wavepacket dispersion rate is nearly six times larger than the one reported for hBN in [29]. This enhanced dispersion suggests that the excited electron-hole wavepackets are more localized in our case, therefore the dispersion rate is larger. We interpret this as consequence of the different excitation mechanisms for each species. In graphene, the non-adiabatic electron-hole excitation results in a broad wavepacket in the reciprocal space, around the Dirac points. In contrast, tunnel excitation, as is the case of hBN, is very sensitive to the band gap, therefore resulting in narrower wavepackets in the reciprocal space around the gap minima.

Finally, in Fig. 3 we show a comparative analysis of the role of ehPR against ehIR for different driving peak intensities. According to the current understanding of HHG in solids, the frequency of the harmonic radiation is given by the energy gap at the time of recombination of the electron-hole pair. Since the trajectories quiver in the reciprocal space with an amplitude ($q_e\mathbf{A}/c$), the harmonic *cutoff* frequency is expected at the maximum gap energy during this excursion. For the two cases represented in Fig. 3, the maximum gap is reached at the turning point ($2q_e\mathbf{A}_0/c$), $\mathbf{A}_0$ being the amplitude of the vector potential. This maximum quivering for each case is represented in the energy band representation in the insets of Fig. 3. According to this, the prediction for the harmonic *cutoff* frequency is the 15th order (≃ 6 eV) for a peak intensity of 1.3×10^{11} (Fig. 3(a)), and the 43rd order (≃ 18 eV) for a peak intensity of 2×10^{12} (Fig. 3(b)), which agrees with the corresponding time-frequency analyses. Figure 3 also shows the prediction of the harmonic emission from the semiclassical SPAM for ehPR (red) and ehIR at distances of 86 Å (green) and 172 Å (grey). As a main observation, we can see that in all cases, ehIR are necessary to reproduce the harmonic emission, specially at longer times. Note that the quiver trajectory of electrons and holes in the reciprocal space is the same for ehPR and ehIR. However, by relaxing the constraint of zero distance at recombination, ehIR harvest the full potential harmonic emission during the quivering, making it possible the emission of the maximum *cutoff* frequency in situations excluded by the ehPR's overlapping constrain.

Optics EXPRESS

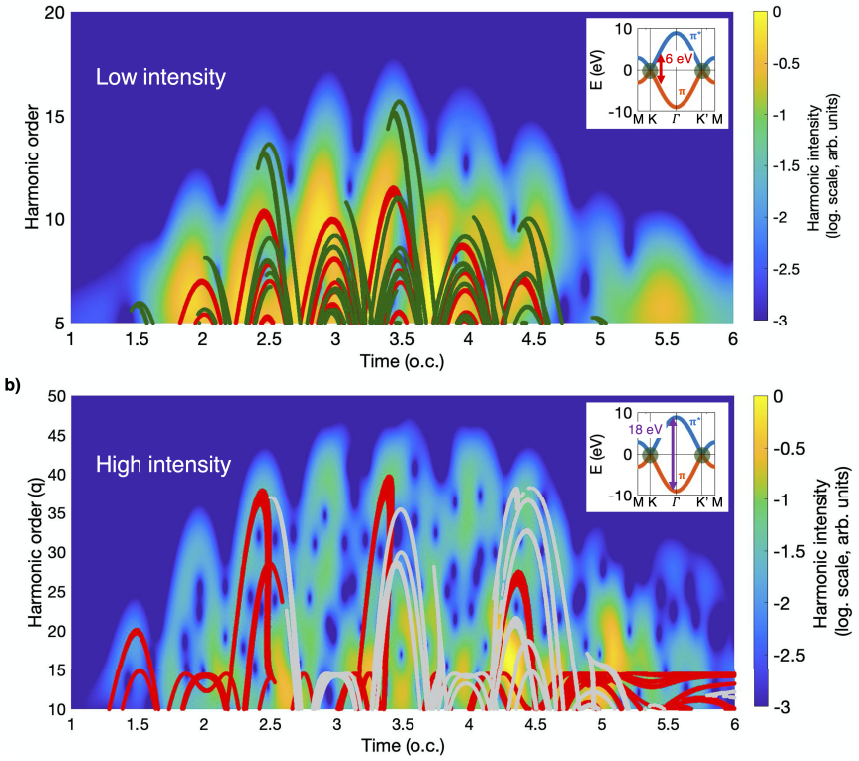

Fig. 3. Time-frequency analysis of the harmonic emission corresponding to two different peak intensities, 1.3×10^{11} W/cm^2 (a) and 2.0×10^{12} W/cm^2 (b), with the same length duration and central wavelength as in the previous figures. For the scan of the spectrum we have used a Gaussian mask of 2.5 ω_0 in (a), and 4 ω_0 in (b). In both panels we plot the frequency of the harmonic emission corresponding to ehPR (red) and to ehIR recombining at 86 Å (green) for (a) and at 172 Å (grey) for (b).

4. Conclusion

We have presented quantum calculations and classical analysis of HHG in single-layer graphene. A comparative analysis with the results of HHG from atoms reveals the extraordinary complex nature of the process in the solid layer. The main trends of the characteristics of this complex emission can be associated with the particular mechanism of HHG in graphene, in which the electron-hole pair excitation is not associated with the maxima of the driving field amplitude. However, our study demonstrates that still relevant spectral features are connected with non-classical recollisions —the so-called *imperfect* recollisions— where the electron-hole pair can recombine even when the classical trajectories do no overlap. We have found that these *imperfect* recollisions typically contribute to the harmonic emission at increasing delayed times for longer recombination distances. These time delays, which are connected with the spreading of the electron and hole wavefunctions to the recombination distance, are significantly larger for graphene. We interpret this result as the consequence of the linear dispersion relation near the Dirac points.

Funding. European Research Council (851201); Ministerio de Educación, Cultura y Deporte (FPU18/03348); FEDER funds (SA287P18); Junta de Castilla y León (SA287P18); Ramón y Cajal (RYC-2017-22745); Ministerio de Ciencia, Innovación y Universidades (PID2019-106910GB-100).

Optics EXPRESS

Acknowledgments. We acknowledge support from the European Research Council (ERC) under the European Union's Horizon 2020 research and innovation programme (grant agreement No. 851201).

Disclosures. "The authors declare no conflicts of interest."

Data availability. Data underlying the results presented in this paper are not publicly available at this time but may be obtained from the authors upon reasonable request.

References

1. A. McPherson, G. Gibson, H. Jara, U. Johann, T. S. Luk, I. A. McIntyre, K. Boyer, and C. K. Rhodes, "Studies of multiphoton production of vacuum-ultraviolet radiation in the rare gases," J. Opt. Soc. Am. B **4**(4), 595–601 (1987).
2. M. Ferray, A. L'Huillier, X. F. Li, L. A. Lompre, G. Mainfray, and C. Manus, "Multiple-harmonic conversion of 1064 nm radiation in rare gases," J. Phys. B: At., Mol. Opt. Phys. **21**(3), L31–L35 (1988).
3. F. Krausz and M. Ivanov, "Attosecond physics," Rev. Mod. Phys. **81**(1), 163–234 (2009).
4. T. Popmintchev, M. C. Chen, D. Popmintchev, P. Arpin, S. Brown, S. Alisauskas, G. Andriukaitis, T. Balciunas, O. Mücke, A. Pugzlys, A. Baltuska, B. Shim, S. E. Schrauth, A. Gaeta, C. Hernández-García, L. Plaja, A. Becker, A. Jaron-Becker, M. M. Murnane, and H. C. Kapteyn, "Bright coherent ultrahigh harmonics in the kev x-ray regime from mid-infrared femtosecond lasers," Science **336**(6086), 1287–1291 (2012).
5. L. Plaja, R. Torres, and A. Zaïr, "Attosecond physics," in *Attosecond Measurements and Control of Physical Systems*, (Springer-Verlag, 2013).
6. S. Ghimire and D. A. Reis, "High-harmonic generation from solids," Nat. Phys. **15**(1), 10–16 (2019).
7. X. Shi, C. T. Liao, Z. Tao, E. Cating-Subramanian, M. M. Murnane, C. Hernández-García, and H. C. Kapteyn, "Attosecond light science and its application for probing quantum materials," J. Phys. B: At., Mol. Opt. Phys. **53**(18), 184008 (2020).
8. K. J. Schafer, B. Yang, L. F. DiMauro, and K. C. Kulander, "Above threshold ionization beyond the high harmonic cutoff," Phys. Rev. Lett. **70**(11), 1599–1602 (1993).
9. K. S. Budil, P. Salières, A. L'Huillier, T. Ditmire, and M. D. Perry, "Influence of ellipticity on harmonic generation," Phys. Rev. A **48**(5), R3437–R3440 (1993).
10. C. Hernández-García, J. A. Pérez-Hernández, T. Popmintchev, M. M. Murnane, H. C. Kapteyn, A. Jaron-Becker, A. Becker, and L. Plaja, "Zeptosecond high harmonic kev x-ray waveforms driven by midinfrared laser pulses," Phys. Rev. Lett. **111**(3), 033002 (2013).
11. C. Hernández-García and L. Plaja, "Resolving multiple rescatterings in high-order-harmonic generation," Phys. Rev. A **93**(2), 023402 (2016).
12. P. C. Li, Y. L. Sheu, H. Z. Jooya, X. X. Zhou, and S. I. Chu, "Exploration of laser-driven electron-multirescattering dynamics in high-order harmonic generation," Sci. Rep. **6**(1), 32763 (2016).
13. J. Tate, T. Auguste, H. G. Muller, P. Salières, P. Agostini, and L. F. DiMauro, "Scaling of wave-packet dynamics in an intense midinfrared field," Phys. Rev. Lett. **98**(1), 013901 (2007).
14. M. V. Frolov, N. L. Manakov, and A. F. Starace, "Wavelength scaling of high-harmonic yield: Threshold phenomena and bound state symmetry dependence," Phys. Rev. Lett. **100**(17), 173001 (2008).
15. J. A. Pérez-Hernández, L. Roso, and L. Plaja, "Harmonic generation beyond the strong-field approximation: the physics behind the short-wave-infrared scaling laws," Opt. Express **17**(12), 9891–9903 (2009).
16. S. Ghimire, A. D. DiChiara, E. Sistrunk, P. Agostini, L. F. DiMauro, and D. A. Reis, "Observation of high-order harmonic generation in a bulk crystal," Nat. Phys. **7**(2), 138–141 (2011).
17. H. Liu, Y. Li, Y. You, S. Ghimire, T. F. Heinz, and D. A. Reis, "High-harmonic generation from an atomically thin semiconductor," Nat. Phys. **13**(3), 262–265 (2017).
18. T. T. Luu, M. Garg, S. Y. Kruchinin, A. Moulet, M. T. Hassan, and E. Goulielmakis, "Extreme ultraviolet high-harmonic spectroscopy of solids," Nature **521**(7553), 498–502 (2015).
19. M. Hohenleutner, F. Langer, O. Schubert, M. Knorr, U. Huttner, S. W. Koch, M. Kira, and R. Huber, "Real-time observation of interfering crystal electrons in high-harmonic generation," Nature **523**(7562), 572–575 (2015).
20. A. A. Lanin, E. A. Stepanov, A. B. Fedotov, and A. M. Zheltikov, "Mapping the electron band structure by intraband high-harmonic generation in solids," Optica **4**(5), 516–519 (2017).
21. O. Schubert, M. Hohenleutner, F. Langer, B. Urbanek, C. Lange, U. Huttner, D. Golde, T. Meier, M. Kira, S. W. Koch, and R. Huber, "Sub-cycle control of terahertz high-harmonic generation by dynamical bloch oscillations," Nat. Photonics **8**(2), 119–123 (2014).
22. N. Tancogne-Dejean and A. Rubio, "Atomic-like high-harmonic generation from two-dimensional materials," Sci. Adv. **4**(2), eaao5207 (2018).
23. A. García-Cabrera, C. Hernández-García, and L. Plaja, "Ultrafast sub-nanometer matter-wave temporal talbot effect," New J. Phys. **23**(9), 093011 (2021).
24. G. Vampa, C. R. McDonald, G. Orlando, D. D. Klug, P. B. Corkum, and T. Brabec, "Theoretical analysis of high harmonic generation in solids," Phys. Rev. Lett. **113**(7), 073901 (2014).
25. G. Ndabashimiye, S. Ghimire, M. Wu, D. A. Browne, K. J. Schafer, M. B. Gaarde, and D. A. Reis, "Solid-state harmonics beyond the atomic limit," Nature **534**(7608), 520–523 (2016).
26. I. Floss, C. Lemell, G. Wachter, V. Smejkal, S. A. Sato, X. M. Tong, K. Yabana, and J. Burgdörfer, "*Ab initio* multiscale simulation of high-order harmonic generation in solids," Phys. Rev. A **97**(1), 011401 (2018).

Optics EXPRESS

27. T. Higuchi, M. I. Stockman, and P. Hommelhoff, "Strong-field perspective on high-harmonic radiation from bulk solids," Phys. Rev. Lett. **113**(21), 213901 (2014).
28. T. T. Luu and H. J. Wörner, "High-order harmonic generation in solids: A unifying approach," Phys. Rev. B **94**(11), 115164 (2016).
29. L. Yue and M. B. Gaarde, "Expanded view of electron-hole recollisions in solid-state high-order harmonic generation: Full-brillouin-zone tunneling and imperfect recollisions," Phys. Rev. A **103**(6), 063105 (2021).
30. O. Zurrón, A. Picón, and L. Plaja, "Theory of high-order harmonic generation for gapless graphene," New J. Phys. **20**(5), 053033 (2018).
31. O. Zurrón-Cifuentes, R. Boyero-García, C. Hernández-García, and L. Plaja, "High harmonic generation in armchair carbon nanotubes," Opt. Express **28**(13), 19760–19771 (2020).
32. N. Yoshikawa, T. Tamaya, and K. Tanaka, "High-harmonic generation in graphene enhanced by elliptically polarized light excitation," Science **356**(6339), 736–738 (2017).
33. S. Jiang, H. Wei, J. Chen, C. Yu, R. Lu, and C. D. Lin, "Effect of transition dipole phase on high-order-harmonic generation in solid materials," Phys. Rev. A **96**(5), 053850 (2017).
34. C. Liu, Y. Zheng, Z. Zeng, and R. Li, "Driving-laser ellipticity dependence of high-order harmonic generation in graphene," Phys. Rev. A **97**(6), 063412 (2018).
35. O. Zurrón-Cifuentes, R. Boyero-García, C. Hernández-García, A. Picón, and L. Plaja, "Optical anisotropy of non-perturbative high-order harmonic generation in gapless graphene," Opt. Express **27**(5), 7776–7786 (2019).
36. Z. Chen and R. Qin, "Circularly polarized extreme ultraviolet high harmonic generation in graphene," Opt. Express **27**(3), 3761–3770 (2019).
37. R. E. F. Silva, A. Jimenez-Galan, B. Amorim, O. Smirnova, and M. Ivanov, "Topological strong-field physics on sub-laser-cycle timescale," Nat. Photonics **13**(12), 849–854 (2019).
38. M. S. Mrudul and G. Dixit, "High-harmonic generation from monolayer and bilayer graphene," Phys. Rev. B **103**(9), 094308 (2021).
39. F. Dong, Q. Xia, and J. Liu, "Ellipticity of the harmonic emission from graphene irradiated by a linearly polarized laser," Phys. Rev. A **104**(3), 033119 (2021).
40. D. Baykusheva, A. Chacón, J. Lu, T. P. Bailey, J. A. Sobota, H. Soifer, P. S. Kirchmann, C. Rotundu, C. Uher, T. F. Heinz, D. A. Reisnd, and S. Ghimire, "All-Optical Probe of Three-Dimensional Topological Insulators Based on High-Harmonic Generation by Circularly Polarized Laser Fields," Nano Lett. **21**(21), 8970–8978 (2021).
41. S. A. Sato, H. Hirori, Y. Sanari, Y. Kanemitsu, and A. Rubio, "High-order harmonic generation in graphene: Nonlinear coupling of intraband and interband transitions," Phys. Rev. B **103**(4), L041408 (2021).
42. R. Boyero-García, O. Zurrón-Cifuentes, L. Plaja, and C. Hernández-García, "Transverse phase matching of high-order harmonic generation in single-layer graphene," Opt. Express **29**(2), 2488–2500 (2021).
43. L. Yue and A. M. B. Gaarde, "Imperfect recollisions in high-harmonic generation in solids," Phys. Rev. Lett. **124**(15), 153204 (2020).
44. L. Li, P. Lan, X. Zhu, T. Huang, Q. Zhang, M. Lein, and P. Lu, "Reciprocal-space-trajectory perspective on high-harmonic generation in solids," Phys. Rev. Lett. **122**(19), 193901 (2019).
45. S. Reich, C. Thomsen, and J. Maultzsch, *Carbon Nanotubes: Basic concepts and physical properties* (Wiley-VCH, 2004).
46. M. Breusing, C. Ropers, and T. Elsaesser, "Ultrafast carrier dynamics in graphite," Phys. Rev. Lett. **102**(8), 086809 (2009).
47. M. Bellini, C. Lyngå, A. Tozzi, M. B. Gaarde, T. W. Hänsch, A. L'Huillier, and C. Wahlström, "Temporal coherence of ultrashort high-order harmonic pulses," Phys. Rev. Lett. **81**(2), 297–300 (1998).
48. M. B. Gaarde, F. Salin, E. Constant, P. Balcou, K. J. Schafer, K. C. Kulander, and A. L'Huillier, "Spatiotemporal separation of high harmonic radiation into two quantum path components," Phys. Rev. A **59**(2), 1367–1373 (1999).
49. A. Zaïr, M. Holler, A. Guandalini, F. Schapper, J. Biegert, L. Gallmann, U. Keller, A. S. Wyatt, A. Monmayrant, I. A. Walmsley, E. Cormier, T. Auguste, J. P. Caumes, and P. Salières, "Quantum path interferences in high-order harmonic generation," Phys. Rev. Lett. **100**(14), 143902 (2008).
50. C. Hernández-García and L. Plaja, "Off-axis compensation of attosecond pulse chirp," J. Phys. B: At., Mol. Opt. Phys. **45**(7), 074021 (2012).
51. S. Carlström, J. Preclíková, E. Lorek, E. W. Larsen, C. M. Heyl, D. Paleček, D. Zigmantas, K. J. Schafer, M. B. Gaarde, and J. Mauritsson, "Spatially and spectrally resolved quantum path interference with chirped driving pulses," New J. Phys. **18**(12), 123032 (2016).